processes

MDPI

Article

Synthesis of 2-DOF Decoupled Rotation Stage with FEA-Based Neural Network

Tingting Ye and Yangmin Li *

Department of Industrial and Systems Engineering, The Hong Kong Polytechnic University, Hong Kong SAR 999077, China
* Correspondence: yangmin.li@polyu.edu.hk

Abstract: Transfer printing technology has developed rapidly in the last decades, offering a potential demand for 2-DOF rotation stages. In order to remove decoupling modeling, improve motion accuracy, and simplify the control method, the 2-DOF decoupled rotation stages based on compliant mechanisms present notable merits. Therefore, a novel 2-DOF decoupled rotation stage is synthesized of which the critical components of decoupling are the topological arrangement and a novel decoupled compound joint. To fully consider the undesired deformation of rigid segments, an FEA-based neural network model is utilized to predict the rotation strokes and corresponding coupling ratios, and optimize the structural parameters. Then, FEA simulations are conducted to investigate the static and dynamic performances of the proposed 2-DOF decoupled rotation stage. The results show larger rotation strokes of 4.302 mrad in one-axis actuation with a 1.697% coupling ratio, and 4.184 and 4.151 mrad in two-axis actuation with undesired Rz rotation of 0.014 mrad with fewer actuators than other works. In addition, the first natural frequency of 2151 Hz is also higher, enabling a wider working frequency range.

Keywords: 2-DOF rotation stage; compliant mechanisms; micro manipulation; transfer printing

Citation: Ye, T.; Li, Y. Synthesis of 2-DOF Decoupled Rotation Stage with FEA-Based Neural Network. *Processes* **2023**, *11*, 192. https://doi.org/10.3390/pr11010192

Academic Editors: Yuchu Qin and Peizhi Shi

Received: 29 November 2022
Revised: 3 January 2023
Accepted: 4 January 2023
Published: 6 January 2023

1. Introduction

With the emergence of transfer printing technology in micro/nano-manufacturing, deformable electronics are endowed to be fabricated [1] and enable many novel applications, such as intelligent electronic skin [2], electronic eye camera [3], bendable photovoltaics module [4], etc. Generally, the operating processes of transfer printing can be divided into three steps [5], as shown in Figure 1a. The main modules contain inks, a donor, a stamp, and a substrate. First, inks are mounted releasably on a donor and prepared to be retrieved by an elastomer stamp. Then, the stamp pasted with the inks is moved above a flexible substrate. At last, the inks are printed onto the flexible substrate. In this process, it is likely that the contact interface between the stamp and the donor/substrate suffers uneven force due to the non-parallel nature of the adjacent faces, easily resulting in poor fabricating quality [6]. To adjust the angle between the adjacent faces, Figure 1b shows a potential application of the 2-DOF (degree of freedom) rotation stage, on which the donor/substrate can be assembled.

Kinematic coupling and positioning precision are issues of great concern in the topological design of the 2-DOF rotation stage. Whether the 2-DOF motions are coupled or not is an important influencing factor in terms of control complexity. As for the decoupled 2-DOF rotation stages proposed by Liang and Lee et al. [7,8], two or four actuators are required, and the 2-DOF rotation motions are not coupled because the arranged planes of actuators are both perpendicular to the installation platform and each other, i.e., the actuators are arranged on the xoz and yoz planes, as shown in Figure 1b. In contrast, the coupled 2-DOF rotation stages developed by Li and Kim et al. [9,10] need three evenly arranged actuators to achieve coupled 2-DOF rotation motions, causing demand for coupled models and increasing control complexity. Concerning positioning precision, compliant mechanisms exhibit advantages over traditional rigid mechanisms since the former realize the transmission of motion and force through elastic deformation of joints, inducing frictionless and gapless situations [11–13].

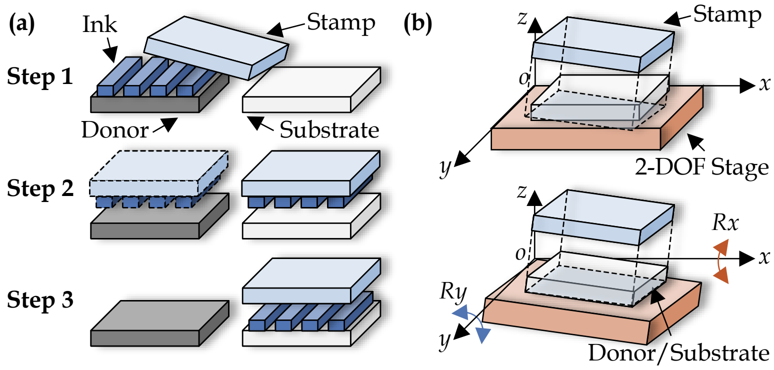

Figure 1. Schematic of transfer printing and potential application of 2-DOF rotation stage in this field. (**a**) Illustration of the operating process of transfer printing. Step 1: some releasable inks are mounted on a donor; Step 2: the inks are retrieved by an elastomer stamp and moved above a substrate; Step 3: the inks are printed onto the substrate. (**b**) Potential application of 2-DOF rotation stage in micro transfer printing.

Given a designed mechanism, the most common design procedure is to predict the performance corresponding to a set of parameters through theoretical modeling and then inverse it, aiming at the desired performance to determine the parameters [14]. Due to the geometric nonlinear deformation and complex series/parallel configuration, the theoretical modeling of compliant mechanisms is faced with considerable challenges [15]. The pseudo-rigid-body method is widely employed to describe the relationship between parameters and performance, whereas its capability to solve large deflection problems is relatively weak, owing to the low accuracy caused by distorted assumptions [16,17]. In the last decade, numerous modeling methods have emerged with higher accuracy, such as the multi-*R* pseudo-rigid-body methods [18,19], improved elliptical integral solutions [20–22], improved constraint beam models [23–26], generalized shooting method [27], etc., which usually comes at the expense of derivation simplicity, computational efficiency, ease of use, etc. What is more, insufficient model descriptiveness usually leads to local optimum problems due to the wide design domain. Inspired by machine learning's strong capability for mine mapping relationships from large-scale data, several machine learning methods have been utilized to solve the synthesis of the graphene kirigami by convolution neural networks [28], the brittle polymers with super-compressible metamaterials by Bayesian neural networks [29], etc. However, rare applications have been conducted in synthesizing compliant mechanisms. Liu et al. employed neural networks for modeling and optimizing the constant force compliant mechanism composed of flexure beams with uneven cross sections based on FEA simulations [30].

Motivated by reducing the hardware costs, simplifying the control methods, and making the motion more precise during transfer printing, a 2-DOF piezo-actuated decoupled rotation stage is synthesized with FEA-based neural networks for a large rotation stroke with high precision and a small coupling ratio, which can serve as a substrate as shown in Figure 1. With comparisons of static and dynamic performances with other piezo-actuated rotation stages, the developed 2-DOF rotation stage shows a larger rotation stroke and a lower coupling ratio with fewer actuators, making control simpler and more precise. Its first natural frequency presents as quite higher than others, resulting in a wider working frequency range. The main contributions of this paper are as follows: (1) A decoupled compound joint is proposed to realize 2-DOF pure rotation motion. (2) A novel piezo-actuated 2-DOF decoupled rotation stage is designed with the proposed decoupled compound joints, 2-DOF rotation hinge, bridge-type amplifiers, work platform, etc., as the main components. (3) Applications of machine learning in the synthesis of compliant mechanisms are expanded. The remainder of this paper is organized as follows. The mechanism design of the 2-DOF decoupled rotation stage is conducted in Section 2, of which the dominant performance results are predicted by the neural network model in Section 3. At last, the FEA simulation is carried out to validate the static and dynamic performance results in Section 4.

2. Mechanism Design

A monolithic 2-DOF decoupled rotation stage is proposed, which comprises a work platform, two decoupled compound joints, a 2-DOF rotation hinge, two piezoelectric stacks, two preload screws, two bridge-type amplifiers, a pillar, and a fixed base, as shown in Figure 2. The topology is symmetrical, of which the central symmetry plane forms an angle of 45° with the two planes xoz and yoz. Taking the left half of Figure 2 as an example, the topological arrangement and motion transmission are as follows.

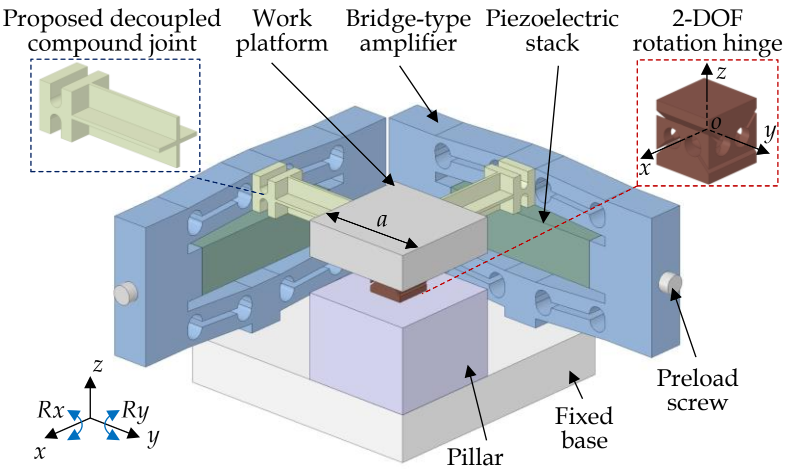

Figure 2. Mechanism of 2-DOF decoupled rotation stage.

As for the topological arrangement, the lower side of the bridge-type amplifier is connected to the fixed base. The piezoelectric stack is assembled inside the bridge-type amplifier, and preloaded by the screw on its polarization direction (i.e., input displacement direction). The work platform is connected with the pillar by the 2-DOF rotation hinge and the bridge-type amplifier with the decoupled compound joint. As for the motion transmission, the polarization direction of the piezoelectric stack is parallel to axis x. The piezoelectric stacks composed of several piezoelectric sheets are chosen as the actuators to provide input displacement and force for the proposed stage due to the merits of high precision and fast response. Through the bridge-type amplifier, the displacement direction in its output end is in axis z. Several parallelogram mechanisms are utilized in bridge-type amplifiers to avoid parasitic displacements of their output ends in axis x. Then, taking the 2-DOF (Rx and Ry) rotation hinge [7,31] as the rotational center of the work platform, the output displacement of the bridge-type amplifier brings the Rx decoupled rotation motion of the working platform through the proposed decoupled compound joint.

To realize 2-DOF (Rx and Ry) decoupled rotation motions, the critical components comprise the topological arrangement and the proposed decoupled compound joint. The decoupled compound joint is composed of a 1-DOF rotation hinge and two perpendicular thin beams. When only the left piezoelectric stack is working, the 1-DOF (Rx) rotation hinge in the left decoupled compound joint is deformed, and the two perpendicular thin beams are undeformed approximately, owing to the high stiffnesses in the directions of Rx and Ry. Meanwhile, the 1-DOF (Ry) rotation hinge in the right decoupled compound joint is undeformed, and the two perpendicular thin beams have rotations in the direction Rx.

3. FEA-Based Neural Network Model

In this section, a neural network model based on FEA is utilized to predict the dominant performance of the proposed 2-DOF decoupled rotation stage precisely, including the rotation strokes and corresponding coupling ratios, as shown in Figure 3.

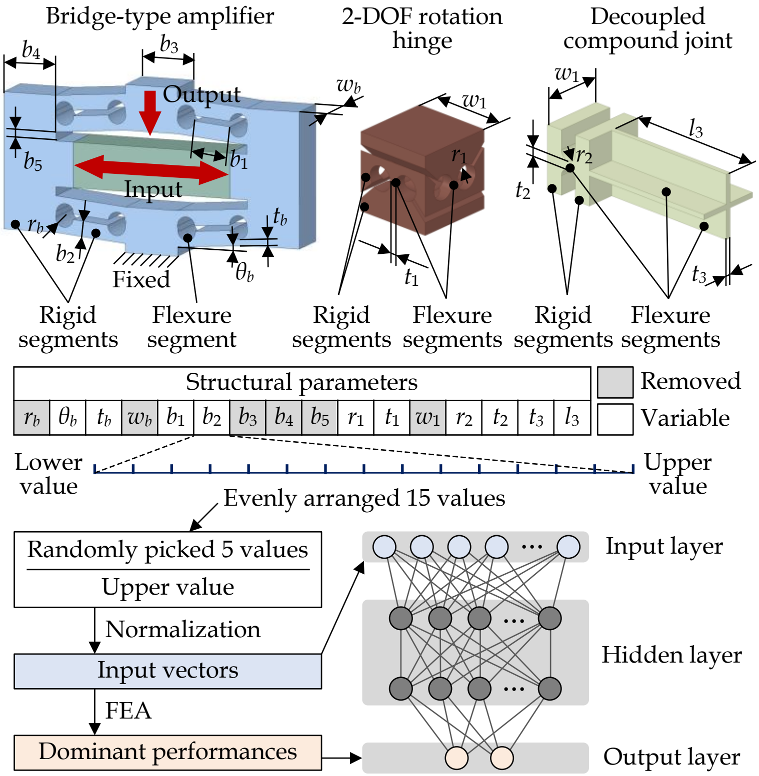

Figure 3. FEA-based neural network model.

Despite the side length a of the work plane set as 12 mm, 16 structural parameters exist. However, N^{16} sets of input vectors mean an extremely huge volume, resulting in high computational costs. Therefore, six less influential parameters, r_b, w_b, b_3, b_4, b_5, and w_1, were assigned specific values based on past experience, as shown in Table 1. Moreover, the lower and upper values of the parameters associated with flexible hinges are related to design experience, relevant literature, and manufacturing limitations. According to the set of upper values, the normalized parameters are used for the input layer of the neural network model. Moreover, the minimum value of each parameter is set as the lower limit. For each parameter, 15 values are taken evenly in their designed range. Among them, five values are picked randomly to create 5^{10} sets of input vectors as the input layer of training data sets.

Table 1. Range or assigned value of structural parameters.

Parameter	Assigned Value	Parameter	Lower Value	Upper Value
a	12 mm	θ_b	0.5°	8°
r_b	1 mm	t_b	0.2 mm	1 mm
w_b	5 mm	b_1	1 mm	10 mm
b_3	4 mm	b_2	1.5 mm	4.5 mm
b_4	6 mm	r_1	0.5 mm	1.5 mm
b_5	1 mm	t_1	0.3 mm	0.9 mm
w_1	3.8 mm	r_2	0.5 mm	1.5 mm
		t_2	0.3 mm	0.9 mm
		t_3	0.3 mm	0.9 mm
		l_3	3 mm	10 mm

Through FEA with the software ANSYS, the dominant performances can be obtained and served as the output layer of the neural network model. The employed material is AL 7075-T651, whose mechanical properties are presented in Table 2. The finite element model is set up with the element sizes as 0.1 mm in flexure segments (i.e., the segments that will deform during work, including all flexure hinges and flexure beams) and 0.5 mm in rigid segments (i.e., the segments that hardly deform during work), as shown in Figure 3. In particular, the 2-DOF rotation hinge is considered a complete flexure segment due to spatial overlap and small size. According to the element quality $Q \in [0, 1]$ that corresponds to the higher quality when the value is bigger obtained by the mesh metric module in ANSYS, more than 92% elements gain their assessed values of more than 0.7, which can prove that the mesh division is reasonable.

Table 2. Mechanical properties of AL 7075-T651.

Item	Density	Poisson's Ratio	Young's Modulus	Yield Strength	Tensile Strength
Parameter	2.810	0.33	71.7	500	570
Unit	g·cm^{-3}		Gpa	Mpa	Mpa

In this work, the neural network model is trained in the software MATLAB. During the training process, several deep neural networks with various hidden layers are considered: the size of the input layer is 10 × 1, the size of the output layer is 2 × 1, and the size of the hidden layer is varied. Two types of loss functions are tried to evaluate the performance of the neural networks, including the mean squared error and the mean absolute percentage error. The employed activation functions compromise the Sigmund activation function, the Gaussian error linear unit activation function, and the Softplus activation function. The stochastic gradient descent optimizer and the Adam optimizer are tried. After considerable trial and appropriate adjustments, the hidden layers with the size of 542 × 1 and 328 × 1 are determined. The mean squared error is assigned as the loss function. The Sigmund activation function is served as the activation function in the input-hidden transmission and the hidden-hidden transmission. The linear activation function is served as the activation function in the hidden-output transmission. The Adam optimizer is employed.

After training with 5^{10} times, the neural network model is tested with four values outside the input data set of each parameter, which are chosen randomly in the designed range. The comparisons of the one-axis rotation stroke and maximum coupling ratio between results by the neural network model and FEA simulation are shown in Figure 4. It can be seen that the overlapping areas of rotation stoke and maximum coupling ratio between the training set and the test set are quite high, which can prove that the neural network model fits the data set well. Moreover, the ratios of the results predicted by the neural network model to those simulated by FEA are 1:1 approximately, which shows that the current neural network model is sufficient for predicting and optimizing the dominant performance of the proposed 2-DOF decoupled rotation stage.

Then, the genetic algorithm is utilized with the function *gamultiobj* in MATLAB to optimize the structural parameters. The upper and lower values refer to Table 1. The optimization objective function is defined as

$$\min \begin{cases} \sigma_1 = -\theta_R, \\ \sigma_2 = \gamma_R, \end{cases} \tag{1}$$

where θ_R is the one-axis rotation stroke, and γ_R is the maximum coupling ratio.

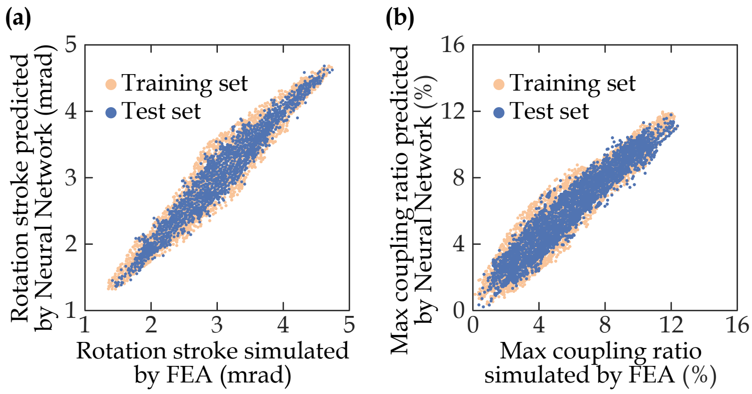

Figure 4. Comparisons of the one-axis rotation stroke and maximum coupling ratio between results by neural network model and FEA. (**a**) Rotation stroke in y-axis actuation. (**b**) Maximum coupling ratio in y-axis actuation.

Consequently, several Pareto front solutions can be obtained by calculation. The solution with relatively small coupling is preferred, and the optimized parameters are shown in Table 3.

Table 3. Optimized structural parameters.

Parameter	Value	Parameter	Value	Parameter	Value
θ_b	3.5°	t_b	0.6 mm	b_1	5.02 mm
b_2	1.6 mm	r_1	0.6 mm	t_1	0.3 mm
r_2	0.5 mm	t_2	0.5 mm	t_3	0.3 mm
l_3	8.2 mm				

4. Characteristic Analysis

To evaluate the performance of the proposed 2-DOF decoupled rotation stage with structural parameters in Table 3, FEA simulation is conducted with the software ANSYS.

4.1. Static Performances

4.1.1. Static Performances without Load

(1) One-axis actuation

The fixed supports are set to the bottom face of the fixed base and one of the input ends of the piezoelectric stack, while the other input ends of the piezoelectric stack are assigned the input displacements with 20 µm to investigate the rotation stroke and corresponding decoupled behavior in one-axis actuation. Through FEA with ANSYS, the static performance results in the y-axis actuation are shown in Figure 5. It can be seen that the y-direction deformation of nodes A, B and D are 25.948, −25.681, and −26.564 µm, as shown in Figure 5a. Since the side length of the work platform is 12 mm, the Ry rotation stroke in y-axis actuation can be derived as 4.302 mrad. As for the decoupled performances, the coupling rotation angles in Rx and Rz can be calculated as 0.073 and 0.061 mrad, according to the y-direction deformations of nodes A and B in Figure 5b. That is, the coupling ratios of Rx and Rz rotations in y-axis actuation are 1.697% and 1.418%. In addition, the amplifying ratio of the bridge-type amplifier is derived as 4.002. Then, the z-direction deformations of nodes A and B present as linear with the input displacement assigned as 2 µm/s, as shown in Figure 5c.

With the maximum input displacement of 20 µm, the maximum equivalent stress occurs at the exact center of the 2-DOF rotation hinge as 207.182 Mpa, which is far less than the yield strength of AL 7075-T651 as 500 Mpa. The maximum equivalent stress of the bridge-type amplifier is located at the half-circular flexure hinge as 155.941 Mpa, and the counterpart of the decoupled compound joint is located at the circular flexure hinge as 69.315 Mpa.

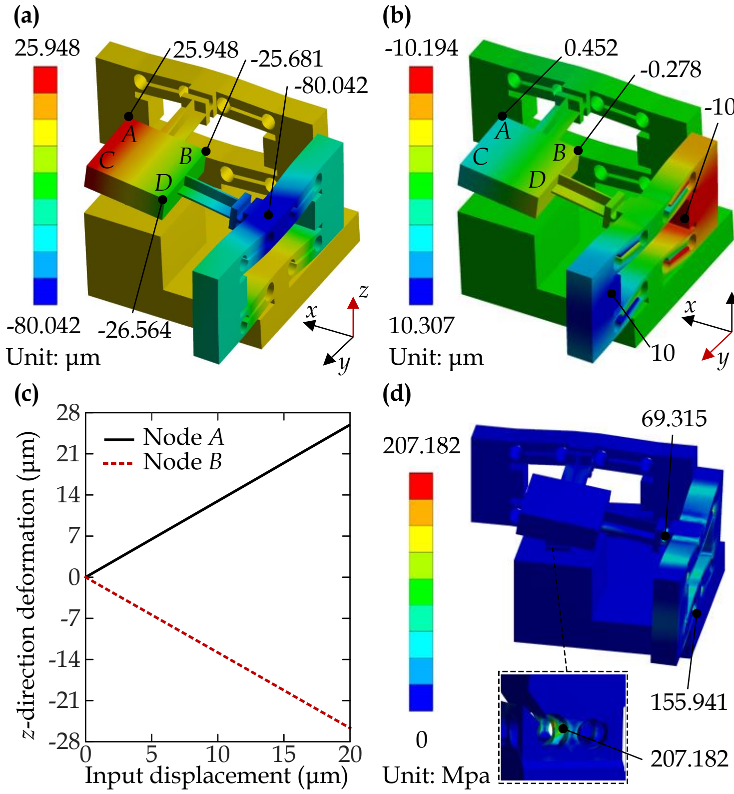

Figure 5. Static performance results in y-axis actuation without load. (**a**) z-direction deformation in y-axis actuation. (**b**) y-direction deformation in y-axis actuation. (**c**) z-direction deformation of nodes A and B in y-axis actuation. (**d**) Stress distribution in y-axis actuation.

(2) Two-axis actuation

As for the two-axis actuation, the fixed supports are set to the bottom face of the fixed base, while the input ends of two piezoelectric stacks are assigned the input displacements with 20 μm to investigate the rotation strokes and consistency behavior in the two-axis actuation. Through FEA with ANSYS, the static performance results in the two-axis actuation are shown in Figure 6. It can be seen that the y-direction deformation of nodes A, B and C are −0.871, −50.684, and 49.339 μm, as shown in Figure 6a. Since the side length of the work platform is 12 mm, the Rx and Ry rotation strokes can be derived as 4.184 and 4.151 mrad. As for the decoupled performance results, the Rz rotation angle can be calculated as 0.014 mrad, according to the y-direction deformations of nodes A and B in Figure 6b. In addition, the amplifying ratios of the bridge-type amplifiers are derived as 3.954 and 3.952. The inconsistency ratio is 1.008:1, in which the discrepancy between the Rx and Ry rotation motions may be attributed to the counteracting effect of the parasitic rotation displacements. Then, the z-direction deformations of nodes A, B, and C present as linear with the input displacements assigned as 2 μm/s, as shown in Figure 6c.

With the maximum input displacement of 20 μm, the maximum equivalent stress occurs at the exact center of the 2-DOF rotation hinge as 420.221 Mpa, which is less than the yield strength of AL 7075-T651 as 500 Mpa. The maximum equivalent stress of the bridge-type amplifier is located at the half-circular flexure hinge as 134.580 Mpa, and the counterpart of the decoupled compound joint is located at the circular flexure hinge as 95.841 Mpa.

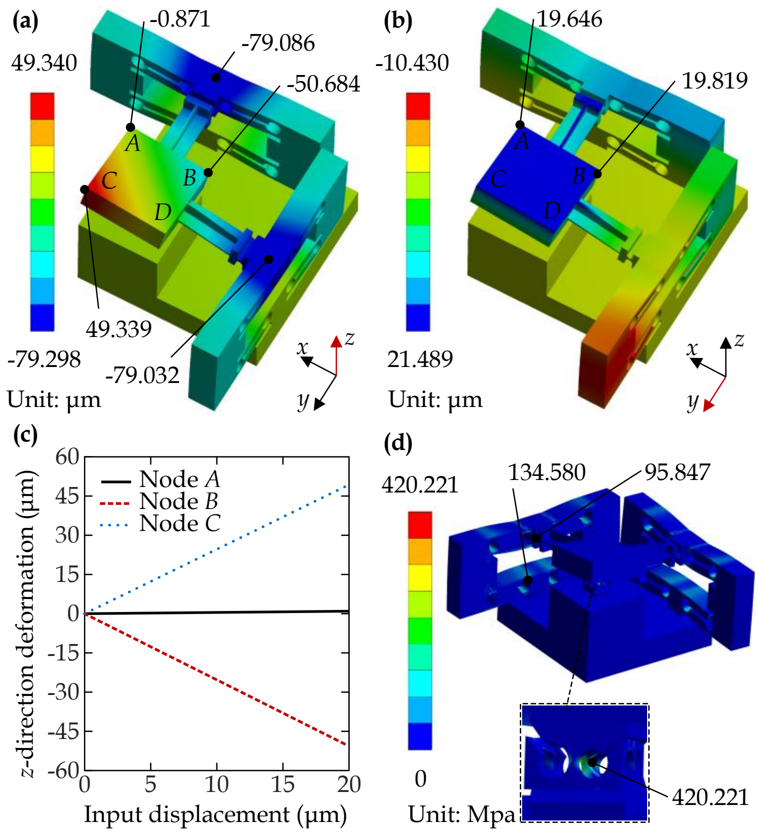

Figure 6. Static performance results in two-axis actuation without load. (**a**) z-direction deformation in x and y-axis actuation. (**b**) y-direction deformation in x and y-axis actuation. (**c**) z-direction deformation of nodes A and B in x and y-axis actuation. (**d**) Stress distribution in x and y-axis actuation.

4.1.2. Static Performance Results with Loads

With loads from 1 N to 5 N applied on the work platform of the proposed stage, the static analyses in one-axis and two-axis actuation are performed. With respect to y-axis actuation with loads from 1 N to 5 N, the rotation motions in directions Rx, Ry, and Rz are shown in Figure 7a. As the load increases, the rotation stroke in the Ry direction decreases, while the coupling rotation motions in the Rx and Rz directions increase. The relationship between the rotation stroke and the load is approximately a straight line with a slope of -6.667×10^{-3} mrad/N. Similarly, the slopes of the straight lines of the coupling rotation motions with respect to the loads are 7.103×10^{-3} mrad/N and 8.919×10^{-4} mrad/N, respectively. In addition, the maximum stress increases from 207.182 MPa to 218.750 Mpa with the growing loads from 0 N to 5 N. As for the x and y-axis actuation with loads from 1 N to 5 N, the rotation motions in directions Rx, Ry, and Rz are shown in Figure 7b. As the load increases, the rotation stroke in the Ry direction decreases, the rotation stroke in the Rx direction increases, and the coupling rotation motion in the Rz direction reduces. The relationships between the rotation motions and the loads are all approximately straight lines. The slopes of the straight lines of the rotation motions in the Rx, Ry, and Rz directions with respect to the loads are 6.420×10^{-3} mrad/N, -6.460×10^{-3} mrad/N, and -6.000×10^{-5} mrad/N, respectively. The maximum stress increases from 420.221 MPa to 454.081 Mpa with the growing loads from 0 N to 5 N. It can be seen that the static performance results of the designed stage possess good stability under loads applied on the work platform from 0 N to 5 N.

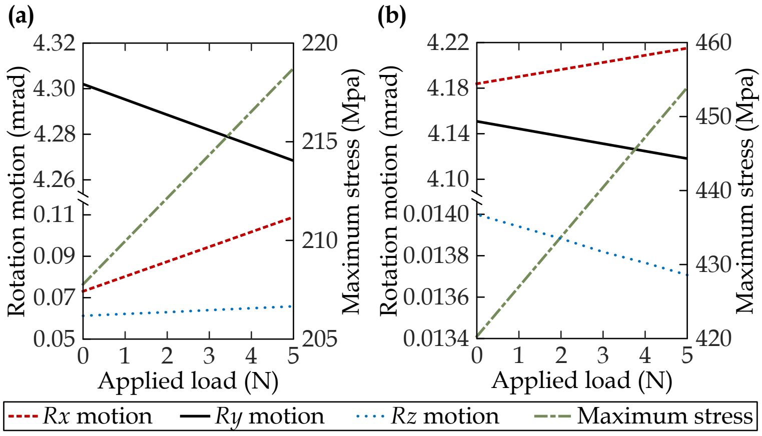

Figure 7. Static performance results with loads. (**a**) Rotation motion and maximum stress in y-axis actuation with loads. (**b**) Rotation motion and maximum stress in x and y-axis actuation.

4.2. Dynamic Performances

With the fixed support on the bottom face of the fixed base, the modal analysis is conducted to the proposed 2-DOF decoupled rotation stage. The first six natural frequencies are 2151, 2154.6, 2194.7, 2432.4, 3175.1, and 3252.2 Hz, respectively. Despite the problem of dense modes due to the symmetric structure, the bandwidth of the 2-DOF decoupled rotation stage covers a fairly high-frequency range. The vibration shapes of the first six modes are shown in Figure 8.

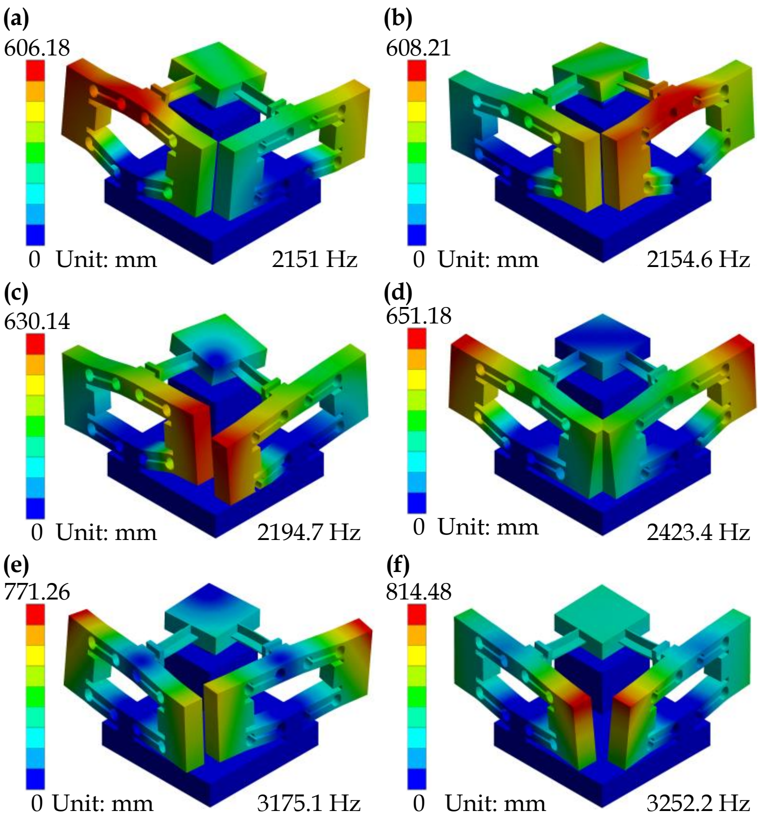

Figure 8. Modal analyses of proposed 2-DOF decoupled stage without loads. (**a**) Total deformation in the first mode (2151 Hz). (**b**) Total deformation in the second mode (2154.6 Hz). (**c**) Total deformation in the third mode (2194.7 Hz). (**d**) Total deformation in the fourth mode (2423.4 Hz). (**e**) Total deformation in the fifth mode (3175.1 Hz). (**f**) Total deformation in the sixth mode (3252.2 Hz).

On this basis, the harmonic responses with actuation frequencies as 100∼3500 Hz in one-axis and two-axis actuation are carried out. For one-axis actuation, the fixed supports are applied on the fixed base and the input ends of one of the piezoelectric stacks, while the input ends of the other piezoelectric stack are assigned input force as 200 N. The y-direction deformations of nodes A and B can be viewed in Figure 9a. Sharp amplitude changes appear around 2100, 2400, and 3200 Hz, which is consistent with the results of the modal analysis. For two-axis actuation, the fixed supports are applied on the fixed base, while the input ends of both piezoelectric stacks are assigned input force as 200 N. The y-direction deformations of nodes A, B, and C can be viewed as Figure 9b. Sharp amplitude changes appear around 2100, 2400, and 3200 Hz, which is consistent with the results of the modal analysis.

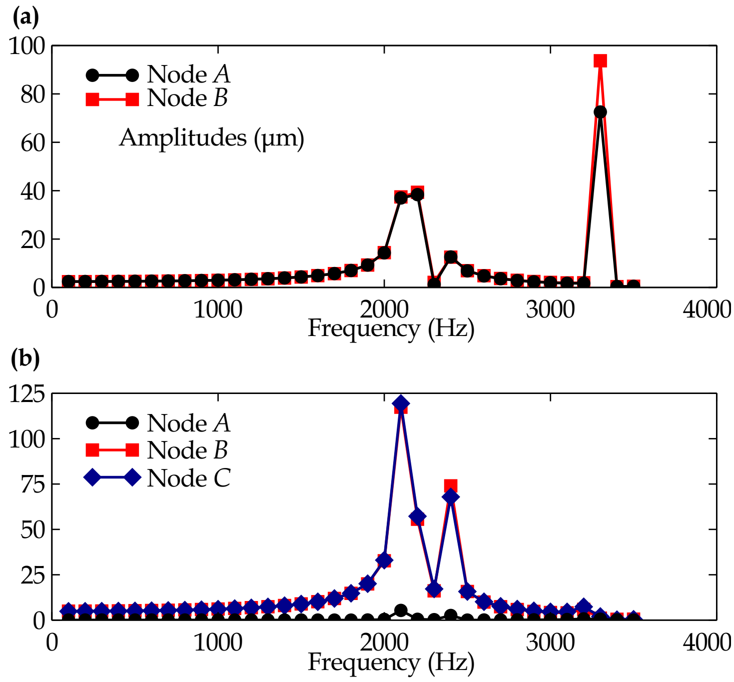

Figure 9. Harmonic responses of proposed 2-DOF decoupled stage. (**a**) y-direction deformation in y-axis actuation. (**b**) y-direction deformation in x and y-axis actuation.

In addition, the modal analyses of the designed stage under loads are conducted, in which the volumes of the cuboids assembled on the work platform are $10 \times 10 \times 3$ mm^3 ($0.3V$) and $10 \times 10 \times 10$ mm^3 (V). The first six natural frequencies $f_i (i = 1{\sim}6)$ of the designed stage without and with loads are shown in Table 4, where ρ denotes the density of Al7075-T651.

Table 4. The first six natural frequencies $f_i (i = 1 \sim 6)$ of the designed stage without and with loads.

Loads	f_1 (Hz)	f_2 (Hz)	f_3 (Hz)	f_4 (Hz)	f_5 (Hz)	f_6 (Hz)
0	2151.0	2154.6	2194.7	2423.4	3175.1	3252.2
$0.3\rho V$	2005.1	2023.3	2169.3	2410.4	3112.9	3127.4
ρV	1405.8	1457.7	2170.7	2415.0	2858.8	2866.6

4.3. Comparisons of Performances with Other Piezo-Actuated Rotation Stages

Comparisons of performance results of the proposed 2-DOF decoupled rotaion stage with other rotation stages are listed in Table 5. It can be seen that the proposed 2-DOF rotation stage has decoupled function, leading to easier control than coupling stages. The rotation stroke and corresponding coupling ratio of the proposed stage also show better performance results with minimal actuators. As for the dynamic performance, the first natural frequency of the proposed 2-DOF rotation stage presents the highest value, leading to a wider working frequency range.

Table 5. Comparisons of performance results with other piezo-actuated rotation stages.

Decoupling	Stoke (Mrad)	Rotation Coupling Ratio	First Natural Frequency (Hz)	Number of Actuators	Reference
✓	2.12	2.09%	580	2	[7]
✓	4	/	165.5	4	[8]
×	1.03	/	249.6	3	[9]
×	0.5	/	88.1	3	[10]
✓	4.302	1.697%	2151	2	This paper

5. Conclusions

The mechanism design, the FEA-based neural network modeling and optimization, and the FEA simulations of the proposed 2-DOF decoupled rotation stage are conducted in this article. With two piezoelectric stacks arranged at two axes and preloaded by two screws, the developed 2-DOF decoupled rotation stage is composed of two bridge-type amplifiers, two decoupled compound joints, a 2-DOF rotation hinge, a work platform, a pillar, and a fixed base, of which the critical components to realize 2-DOF decoupled rotation motions present as the topological arrangement and the decoupled compound joints. To avoid the neglect of the undesired deformation of rigid segments, an FEA-based neural network model is applied to accurately predict the rotation stroke and the coupling ratio and optimize the structural parameters. At last, the FEA simulations are conducted to evaluate the static and dynamic performance of the proposed 2-DOF stage. Actuated by fewer piezoelectric actuators, it shows larger rotation strokes for 4.302 mrad in one-axis actuation with the 1.697% coupling ratio and 4.184 and 4.151 mrad in the two-axis actuation with undesired Rz rotation of 0.014 mrad compared to other works. A higher first natural frequency of 2151 Hz is displayed, resulting in a wider working frequency range. However, it is respected through the modal analyses under loads that the dynamic performance of the developed stage under loads is not outstanding. Similar problems can also be found in compliant mechanisms with high amplifying ratios or serial connections. In future work, the comprehensive performance will be further considered during the design and optimization process; a prototype of the designed stage will be fabricated and tested to evaluate the static and dynamic performance results.

Author Contributions: Conceptualization, T.Y.; data curation, T.Y.; investigation, T.Y.; methodology, T.Y.; validation, T.Y.; writing—original draft preparation, T.Y.; writing—review and editing, T.Y. and Y.L.; supervision, Y.L. All authors have read and agreed to the published version of the manuscript.

Funding: This research was funded by the ISE DGRF of The Hong Kong Polytechnic University (Project No UAPM).

Institutional Review Board Statement: Not applicable.

Informed Consent Statement: Not applicable.

Data Availability Statement: Not applicable.

Conflicts of Interest: The authors declare no conflict of interest.

Abbreviations

The following abbreviations are used in this manuscript:

DOF	Degree of freedom
FEA	Finite element analysis

References

1. Linghu, C.; Zhang, S.; Wang, C.; Song, J. Transfer printing techniques for flexible and stretchable inorganic electronics. *NPJ Flex. Electron.* **2018**, *2*, 26. [CrossRef]
2. Zhang, S.; Li, S.; Xia, Z.; Cai, K. A review of electronic skin: Soft electronics and sensors for human health. *J. Mater. Chem. B* **2020**, *8*, 852–862. [CrossRef] [PubMed]
3. Tang, X.; Ackerman, M.M.; Shen, G.; Guyot-Sionnest, P. Towards infrared electronic eyes: Flexible colloidal quantum dot photovoltaic detectors enhanced by resonant cavity. *Small* **2019**, *15*, 1804920. [CrossRef] [PubMed]
4. Commault, B.; Duigou, T.; Maneval, V.; Gaume, J.; Chabuel, F.; Voroshazi, E. Overview and perspectives for vehicle-integrated photovoltaics. *Appl. Sci.* **2021**, *11*, 11598. [CrossRef]
5. Zhou, X.; Tian, P.; Sher, C.W.; Wu, J.; Liu, H.; Liu, R.; Kuo, H.C. Growth, transfer printing and colour conversion techniques towards full-colour micro-LED display. *Prog. Quantum Electron.* **2020**, *71*, 100263. [CrossRef]
6. Park, J.; Lee, Y.; Lee, H.; Ko, H. Transfer printing of electronic functions on arbitrary complex surfaces. *ACS Nano* **2020**, *14*, 12–20. [CrossRef]
7. Liang, C.; Wang, F.; Huo, Z.; Shi, B.; Tian, Y.; Zhao, X.; Zhang, D. A 2-DOF monolithic compliant rotation platform driven by piezoelectric actuators. *IEEE Trans. Ind. Electron.* **2019**, *67*, 6963–6974. [CrossRef]
8. Lee, H.J.; Kim, H.C.; Kim, H.Y.; Gweon, D.G. Optimal design and experiment of a three-axis out-of-plane nano positioning stage using a new compact bridge-type displacement amplifier. *Rev. Sci. Instrum.* **2013**, *84*, 115103. [CrossRef]
9. Qu, J.; Chen, W.; Zhang, J.; Chen, W. A piezo-driven 2-DOF compliant micropositioning stage with remote center of motion. *Sens. Actuators A Phys.* **2016**, *239*, 114–126. [CrossRef]
10. Kim, H.; Kim, J.; Ahn, D.; Gweon, D. Development of a nanoprecision 3-DOF vertical positioning system with a flexure hinge. *IEEE Trans. Nanotechnol.* **2013**, *12*, 234–245. [CrossRef]
11. Ling, J.; Ye, T.; Feng, Z.; Zhu, Y.; Li, Y.; Xiao, X. A survey on synthesis of compliant constant force/torque mechanisms. *Mech. Mach. Theory* **2022**, *176*, 104970. [CrossRef]
12. Zhu, B.; Zhang, X.; Zhang, H.; Liang, J.; Zang, H.; Li, H.; Wang, R. Design of compliant mechanisms using continuum topology optimization: A review. *Mech. Mach. Theory* **2020**, *143*, 103622. [CrossRef]
13. Feng, Z.; Liang, W.; Ling, J.; Xiao, X.; Tan, K.K.; Lee, T.H. Precision force tracking control of a surgical device interacting with a deformable membrane. *IEEE/ASME Trans. Mechatron.* **2022**, *27*, 5327–5338. [CrossRef]
14. Bilancia, P.; Berselli, G. An overview of procedures and tools for designing nonstandard beam-based compliant mechanisms. *Comput.-Aided Des.* **2021**, *134*, 103001. [CrossRef]
15. Ling, M.; Howell, L.L.; Cao, J.; Chen, G. Kinetostatic and dynamic modeling of flexure-based compliant mechanisms: A survey. *Appl. Mech. Rev.* **2020**, *72*, 030802. [CrossRef]
16. Chen, W.; Qu, J.; Chen, W.; Zhang, J. A compliant dual-axis gripper with integrated position and force sensing. *Mechatronics* **2017**, *47*, 105–115. [CrossRef]
17. Li, B.; Hao, G. On generating expected kinetostatic nonlinear stiffness characteristics by the kinematic limb-singularity of a crank-slider linkage with springs. *Chin. J. Mech. Eng.* **2019**, *32*, 54. [CrossRef]
18. Yu, Y.Q.; Zhu, S.K. 5R pseudo-rigid-body model for inflection beams in compliant mechanisms. *Mech. Mach. Theory* **2017**, *116*, 501–512. [CrossRef]
19. Šalinić, S.; Nikolić, A. A new pseudo-rigid-body model approach for modeling the quasi-static response of planar flexure-hinge mechanisms. *Mech. Mach. Theory* **2018**, *124*, 150–161. [CrossRef]
20. Holst, G.L.; Teichert, G.H.; Jensen, B.D. Modeling and experiments of buckling modes and deflection of fixed-guided beams in compliant mechanisms. *ASME J. Mech. Des.* **2011**, *133*, 051002. [CrossRef]
21. Ye, T.; Ling, J.; Kang, X.; Feng, Z.; Xiao, X. A novel two-stage constant force compliant microgripper. *ASME J. Mech. Des.* **2021**, *143*, 053302. [CrossRef]
22. Zhang, A.; Chen, G. A comprehensive elliptic integral solution to the large deflection problems of thin beams in compliant mechanisms. *ASME J. Mech. Robot.* **2013**, *5*, 021006. [CrossRef]
23. Chen, G.; Ma, F.; Hao, G.; Zhu, W. Modeling large deflections of initially curved beams in compliant mechanisms using chained beam constraint model. *ASME J. Mech. Robot.* **2019**, *11*, 011002. [CrossRef]
24. Ma, F.; Chen, G. Modeling large planar deflections of flexible beams in compliant mechanisms using chained beam-constraint-model. *ASME J. Mech. Robot.* **2016**, *8*, 021018. [CrossRef]
25. Ma, F.; Chen, G. Bi-BCM: A closed-form solution for fixed-guided beams in compliant mechanisms. *ASME J. Mech. Robot.* **2017**, *9*, 014501. [CrossRef]
26. Chen, G.; Ma, F. Kinetostatic modeling of fully compliant bistable mechanisms using Timoshenko beam constraint model. *ASME J. Mech. Des.* **2015**, *137*, 022301. [CrossRef]
27. Kuo, Y.L.; Lan, C.C. A two-dimensional adjustable constant-force mechanism. *ASME J. Mech. Des.* **2020**, *142*, 063304. [CrossRef]
28. Hanakata, P.Z.; Cubuk, E.D.; Campbell, D.K.; Park, H.S. Accelerated search and design of stretchable graphene kirigami using machine learning. *Phys. Rev. Lett.* **2018**, *121*, 255304. [CrossRef]
29. Bessa, M.A.; Glowacki, P.; Houlder, M. Bayesian machine learning in metamaterial design: Fragile becomes supercompressible. *Adv. Mater.* **2019**, *31*, 1904845. [CrossRef]

30. Liu, F.; Jiang, X.; Wang, X.; Wang, L. Machine learning-based design and optimization of curved beams for multistable structures and metamaterials. *Extrem. Mech. Lett.* **2020**, *41*, 101002. [CrossRef]
31. Farhadi Machekposhti, D.; Tolou, N.; Herder, J.L. A review on compliant joints and rigid-body constant velocity universal joints toward the design of compliant homokinetic couplings. *ASME J. Mech. Des.* **2015**, *137*, 032301. [CrossRef]